http://eprints.gla.ac.uk/193618/

Deposited on: 21 August 2019

Photovoltaic Power Harvesting Technologies in Biomedical Implantable Devices Considering the Optimal Location

Jinwei Zhao, *Student Member, IEEE*, Rami Ghannam, *Senior Member, IEEE*, Man Kay Law, *Senior Member, IEEE*, Muhammad Ali Imran, *Senior Member, IEEE* and Hadi Heidari, *Senior Member*, IEEE
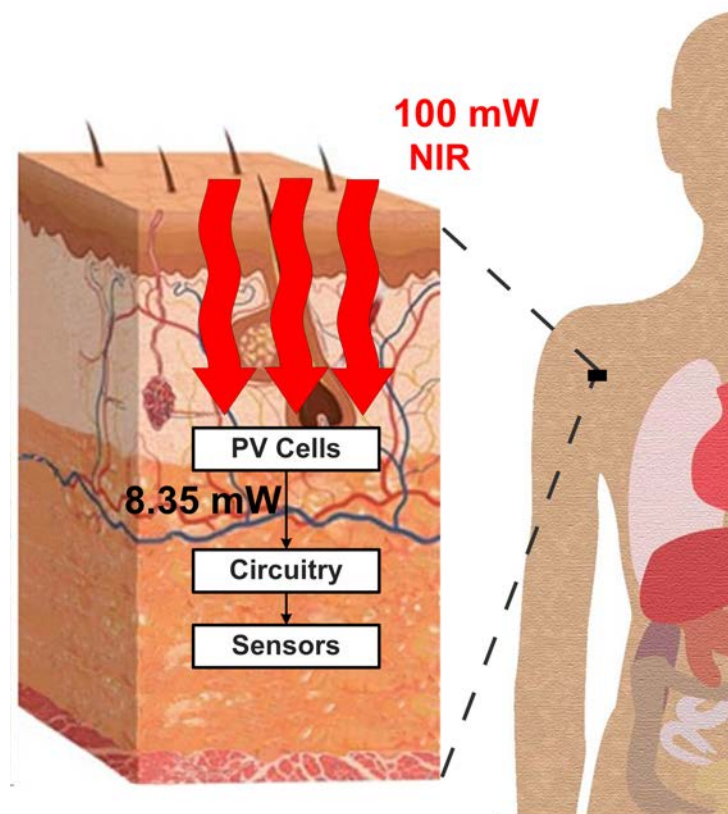
The implantable photovoltaic energy harvesting system implanted in the optimal location.

Take-Home Messages
- This is first time to model the performance of implantable PV cells in different layers of tissue. We demonstrate how the electrical characteristics are influenced by the implanting location of the device.
- A PV cell implanted in the dermis layer can harvest the greatest amount of power.
- We propose implanting our energy harvesting PV cells in the hypodermis layer.
- Our proposed PV device harvests enough energy to supply power for low-cost implants such as cardiac pacemakers, retinal implants or biomedical sensors.
- PV cells implanted in the adipose layer can harvest nearly 11.84 mW using an 850 nm light source.

Photovoltaic Power Harvesting Technologies in Biomedical Implantable Devices Considering the Optimal Location

Jinwei Zhao, *Student Member, IEEE*, Rami Ghannam, *Senior Member, IEEE*, Man Kay Law, *Senior Member, IEEE*, Muhammad Ali Imran, *Senior Member, IEEE* and Hadi Heidari, *Senior Member*, IEEE

Abstract There are still many challenges in effectively harvesting and generating power for implantable medical devices. Most of today's research focuses on finding ways to harvest energy from the human body to avoid the use of batteries, which require surgical replacement. For example, current energy harvesters rely on piezoelectricity, thermoelectricity and solar electricity to drive the implantable device. However, the majority of these energy harvesting techniques suffer from a variety of limitations such as low power output, large size or poor efficiency. Due to their high efficiency, we focus our attention on solar photovoltaic cells. We demonstrate the tissue absorption losses severely influence their performance. We predict the performance of these cells using simulation through the verified experimental data. Our results show that our model can obtain 17.20% efficiency and 0.675 V open-circuit voltage in one sun condition. In addition, our device can also harvest up to 15 mW/cm^2 in dermis and 11.84 mW/cm^2 in hypodermis by using 100 mW/cm^2 light source at 800 nm and 850 nm, respectively. We propose implanting our device in hypodermis to obtain a stable power output.

Keywords — **Implantable Device, Power harvesting, Photovoltaic, Optimal location**

I. INTRODUCTION[1]

Biomedical implantable and wearable devices play a significant role in modern therapy and diagnosis [1]. Due to their clinical demand, a variety of subcutaneous devices such as defibrillators, pacemakers, cochlear implants, drug pumps, neurological stimulators and biomedical sensors are now being developed [2-7]. Power harvesting or generation is still a big challenge in these devices. Due to the hazardous nature of batteries as well as their size, lifespan and the need for surgical replacement, alternative energy generation techniques are now in high demand [8]. Emerging power harvesters include Photovoltaic cells (PV), Piezoelectric Generators (PEG), Thermoelectric Cells (TEG), Biofuel Cells (BC), and Triboelectric nanogenerators (TENG). They can harvest energy from human fluids, the human body or the external environment [9-14]. Another alternative method relies on Wireless Power Transfer (WPT), which enables power transfer between an external power source and an implantable device [15, 16]. The literature has demonstrated the feasibility of implanting these devices in small mammals [8, 17-19], lobsters [20], insects [21, 22] and snails [23], with some research based on in-vitro testing [24-26]. Compared with other power harvesting techniques, WPT enables the device to be implanted in the human body [27] and is approved by the Food and Drug Administration (FDA) [8, 15]. PEG, TEG and TENG are designed to harvest energy produced by body fluids or temperature gradients. All of these require specific locations with high motion or temperature changes. BC is highly biocompatible with living organisms and has been tested with plants, insects and mammals [20-23, 28, 29]. Despite its low output voltage and enzymatic degradation, the abundance of glucose in living organisms makes it a feasible power harvesting technology for implantable devices. In WPT, the near-field inductive coupling method is mostly applied in implantable applications [15]. Large coil size, short power range and tissue loss are still unaddressed challenges [15, 30]. Ultrasonic power harvesting is one way to overcome these drawbacks, but the amount of power is lower than 1 mW [31].

Compared with other technologies, PV cells can produce energy in the tens to hundreds of microwatts range within a relatively small area (mm^2 scale) [26, 32-35]. Previous studies have shown that commercial PV cells are capable of powering an implantable pacemaker [26]. In L. Lu *et al.* 2018 [26], monocrystalline cell arrays were designed and tested under a 4 mm skin layer (2 mm pork skin + 2 mm chicken muscle). Ultrathin and flexible photovoltaic cells were made using biocompatible encapsulation [26].

J. Zhao, R. Ghannam, M. A. Imran and H. Heidari are with the School of Engineering, University of Glasgow, G12 8QQ, Glasgow, United Kingdom (Hadi.Heidari@glasgow.ac.uk).

M. K. Law is with the State Key Laboratory of Analog and Mixed-Signal VLSI, AMSV, Research Building N21, 3/F, University of Macau, Avenida da Universidade, Taipa, Macau, China.
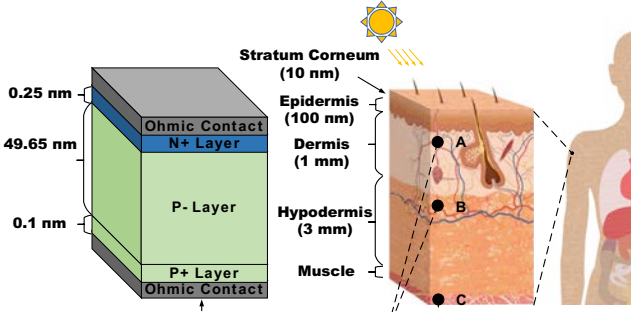
Fig. 1. The implantable photovoltaic energy harvester, of which structure is PPN back-surface illuminated. The device is verified in a multilayer skin model by using FEM macroscopic simulation in COMSOL. A, B and C are the implant locations in our model: A) under epidermis, B) under dermis, and C) under adipose.

Moreover, Hung *et al.* [35] demonstrated that the antireflective Silicon Nanowire (SINW) surface produced by low-temperature surface passivation can improve the output characteristics of CMOS PV cells (Maximum efficiency is 21.84% (under 5 mW/mm^2 condition) and 18.4% (under 0.5 mW/mm^2) without treatment.   Furthermore, the performance of these low-cost thin film PV cells can be significantly improved using various light trapping techniques [35]. Nevertheless, the temperature change from 15 °C to 45 °C can result in 10% output voltage reduction [35]. Similarly, Moon et al. show that an N$^+$P$^-$P$^+$ back-side illuminated crystalline silicon cell can harvest low-flux NIR light in subcutaneous conditions. An efficiency of 17.12% was achieved using a *Si$_3$N$_4$* passivation layer on the illuminated surface [36].

Tissue loss is still a challenge which limits the harvested energy of the PV cells. Maximum transmittance through human tissue occurs in the NIR spectral region. Silicon PV cells can therefore efficiently accumulate and convert energy according to their good response in NIR region [36]. However, the small incident power according to a small active area of implantable PV cell and a high recombination rate in NIR region can massively diminish the output characteristics [32]. Besides, each person's skin type (e.g. ethnic background, gender and age [37-39]) can affect the PV cell's performance. For toxicity, there are some previous works showing feasibility to use silicon PV cells in implantable applications. In L. Lu 2018 *et al.* [26], they implemented an ultrathin integrated solar cell array based on monocrystalline silicon microcells as a power supply, including the active layers, electrodes, interconnections, and encapsulation layers using fully biocompatible and biodegradable materials. In their study, they designed a 7-day in-vivo test in a hairless rat. The cytotoxicity test provides good biocompatibility of the implantable PV cell. The obtained overall viability between 89% and 91% is consistent with an absence of any toxic effects. Throughout the duration of the experiment, the numbers of dead cells are significantly lower than that of the living cells, thereby providing evidence of good biocompatibility.

However, the literature provides little insight into the ideal position of implanting these PV cells. There is also no

mentioning of the optimized device structure, which is important before any fabrication and implantation takes place. Consequently, we will present our optimized 2D PV cell structure using a simulation platform that relies on solving Maxwell's semiconductor equations. In addition, light propagation through the stratum corneum, epidermis, dermis and adipose will be modelled using the Jones matrix technique. Our energy harvesting PV device will be inserted in each of these different layers, as shown in Fig. 1. We will therefore demonstrate the performance of the PV cell when it is placed in different skin locations and skin layers.

A. Semiconductor principles

Most PV cells are fabricated using semiconductor materials such as Si, GaAs and CdTe. According to the literature, organic materials are generating much interest due to their flexibility, low price and low fabrication costs. However, they still suffer from poor stability and a large active area is required due to their low conversion efficiency [40]. Most implantable PV cells are made of crystalline silicon due to their high efficiency and non-toxicity [40]. Consequently, we will therefore focus our study on semiconductor PV cells.

Carrier transport in the semiconductor layers can be simulated by invoking the Poisson and continuity equations (equations 1a and 1c). Moreover, we invoke Snell's law and Maxwell's equations to analyze light penetration using the Jones matrix method [41]. All these equations can be solved using the Finite Element Method (FEM) [42]. Thus,

$$-\nabla \cdot \nabla \psi = \frac{q}{\varepsilon}(p - n + N_D^+ - N_A^-) \qquad (1a)$$

$$\frac{\partial n}{\partial t} = -\mu_n n \nabla^2 \psi + D_n \nabla^2 n + G - R \qquad (1b)$$

$$\frac{\partial p}{\partial t} = \mu_p p \nabla^2 \psi + D_p \nabla^2 p + G - R \qquad (1c)$$

where n and p are the electron and hole concentrations, ψ is the electrostatic potential, q is the electron charge, ε is the permittivity of semiconductor, N_D^+ and N_A^- are the ionized donor and acceptor impurity concentrations, k is the Boltzmann constant, T is the ambient temperature, μ_n and μ_p are the electron and hole mobilities, $D_{n,p}$ are the electron and hole diffusion coefficient ($D_{n,p}=\mu_{n,p}kT/q$), and G and R present the generation rate and recombination rate of electron-hole pairs. The recombination rates (R) are composed of direct radiative (R_{rad}), Auger (R_{Au}) and Shockley-Read-Hall (R_{SRH}) recombination [42]:

$$R_{SRH} = \frac{pn - n_i^2}{\tau_p(n + n_1) + \tau_n(p + p_1)} \qquad (2a)$$

$$R_{Au} = (g_{eeh}C_n n + g_{ehh}C_p p)(pn - n_i^2) \qquad (2b)$$

$$R_{rad} = g_{eh}B(pn - n_i^2) \qquad (2c)$$

where p_1, n_1 are the trap state hole/electron concentration, g_{eh}, g_{eeh} and g_{ehh} are the injection factors, B is the radiative

Global Parameter	Value	Verified model	Value	Our model	Value
X	4.05 eV [47][51]	t_n	0.34 μm [32]	t_{n+}	0.25 μm
E_g	1.124 eV [47]	t_p	35 μm [32]	t_{p-}	49.65 μm
N_c	2.8×10^{19} cm^{-3} [51]	Si_3N_4	100 nm [32]	t_{p+}	0.1 μm
N_v	1.2×10^{19} cm^{-3} [51]	n	2.5×10^{16} cm^{-3}	N^+	1×10^{19} cm^{-3}
D_n	36 cm^2/s [47]	p	2×10^{17} cm^{-3}	P^-	4.6×10^{15} cm^{-3}
D_p	12 cm^2/s [47]	n_i	1.0×10^{10} cm^{-3} [51]	P^+	1×10^{20} cm^{-3}
μ_n	1350 m^2/Vs [51]	$Area$	1.23 mm^2	n_i	1.0×10^{10} cm^{-3} [48]
μ_p	450 m^2/Vs [51]	λ	850 nm	$Area$	1 cm^2
Q	1.6022×10^{19} C [47]	I_0	1.06 μW/mm^2	λ	550 μm
ε_r	11.7 [47]	T	300 K	I_0	1000 W/m^2
$N(Silicon)$	[51]	$\tau_{p,n}$ (N layer)	30 μs [52] [53]	$\tau_{p,n}$ (P- layer)	100 μs [52][53]
$K(Silicon)$	[51]	$\tau_{p,n}$ (P layer)	20 μs [52] [53]	$\tau_{p,n}$ (N+ layer)	80 μs [52] [53]
C_n	2.8×10^{-31} cm^{6}s^{-1} [54]			$\tau_{p,n}$ (P+ layer)	2 ns [49] [53]
C_p	9.9×10^{-32} cm^{6}s^{-1} [54]			$N(stratum\ corneum)$	1.55 [44]
B_{rad}	1.1×10^{-14} cm^{3}s^{-1} [46]			$N(epidermis)$	1.36 [44]
C	2.99×10^8 m/s [47]			$N(dermis)$	1.41 [44]
m_e*/m_e	1.08 [51]			$N(adipose)$	1.44 [44]
m_h*/m_e	0.57 [51]			$K(stratum\ corneum)$	[44]
Δ	0.0426 eV [47]			$K(epidermis)$	[44]
θ	0			$K(dermis)$	[44]
				$K(adipose)$	[44]

This table indicates the parameters used in our device model for verification.

coefficient, C_n and C_p are the Auger coefficients, τ_p and τ_n are the recombination lifetimes. The generation rate can be determined by [41]:

$$G(\lambda) = \alpha(\lambda)b(\lambda)P_s(x, y, \lambda) \qquad (3)$$

where $\alpha(\lambda)$ is the absorption coefficient of semiconductor, $b(\lambda)$ is the photon flux on the surface, P_s is the power flow according to various wavelengths and the depth into the device in x- and y- direction. The photon flux can be calculated from the light intensity of Air Mass 1.5 Global (AM1.5G).

B. Initial and boundary conditions

To begin, we apply the neutral charge condition to setup the doping profile and ohmic contact characteristics for estimating the initial electrostatic potential [41]. In our model, we enable periodic boundary conditions to analyze carrier diffusion and electrical potentials in the transverse directions. The Neumann boundary conditions are applied to separate the simulation domains. The fluxes across the boundaries were set to zero ($ñ·E=0$, $ñ·J_{n,p}=0$, $ñ·S_{n,p}=0$), where $ñ$ is the outward-oriented vector.

C. Performance Characteristics

The electron current (J_n), hole current (J_p) and short-circuit current (J_{sc}) can be determined using [41, 42]:

$$J_n = -q\mu_n n\nabla\psi + qD_n\nabla n \qquad (4a)$$

$$J_p = -q\mu_p p\nabla\psi - qD_p\nabla p \qquad (4b)$$

$$J_{sc} = \iiint_{\lambda\ y\ x} \left| J_n(x,y,\lambda) + J_p(x,y,\lambda) \right| dxdyd\lambda \quad (4c)$$

Considering the parasitic resistances, the output current density of the PV cell can be obtained using [41]:

$$J(V) = -J_0 e^{-V/V_T} + J_{sc} - \frac{V + J(V)R_s}{R_{sh}} \qquad (5)$$

where R_s and R_{sh} are the series and shunt parasitic resistances, and V_T is the thermal voltage ($V_T=kq/T$). Since our simulation model is in 2D, R_s can be neglected and R_{sh} can be calculated using the IV characteristic of the device. The External Quantum Efficiency (EQE) can be determined using [41, 42]:

$$EQE = \frac{hcJ_{sc}}{q\lambda P_{in}} \qquad (6)$$

where h is the Plank constant, c is the speed of light, P_{in} is the input power flux density (AM 1.5G light intensity).

A. Skin Model Description

The amount of electrical energy generated from the photovoltaic effect in subcutaneous conditions is highly related to the thickness and optical properties of skins [43]. In this section, we will demonstrate how we can constructed a model to simulate light propagation through the skin [26, 37, 43, 44]. Skin is composed of a number of layers that include the Stratum corneum, epidermis, dermis and hypodermis (adipose layer). According to K. Song *et al.* 2017 [43], the thickness of each of these skin layers is inhomogeneous [43] and the thickness of the epidermis and dermis are between 32 μm and 1.8 mm, respectively. In fact,
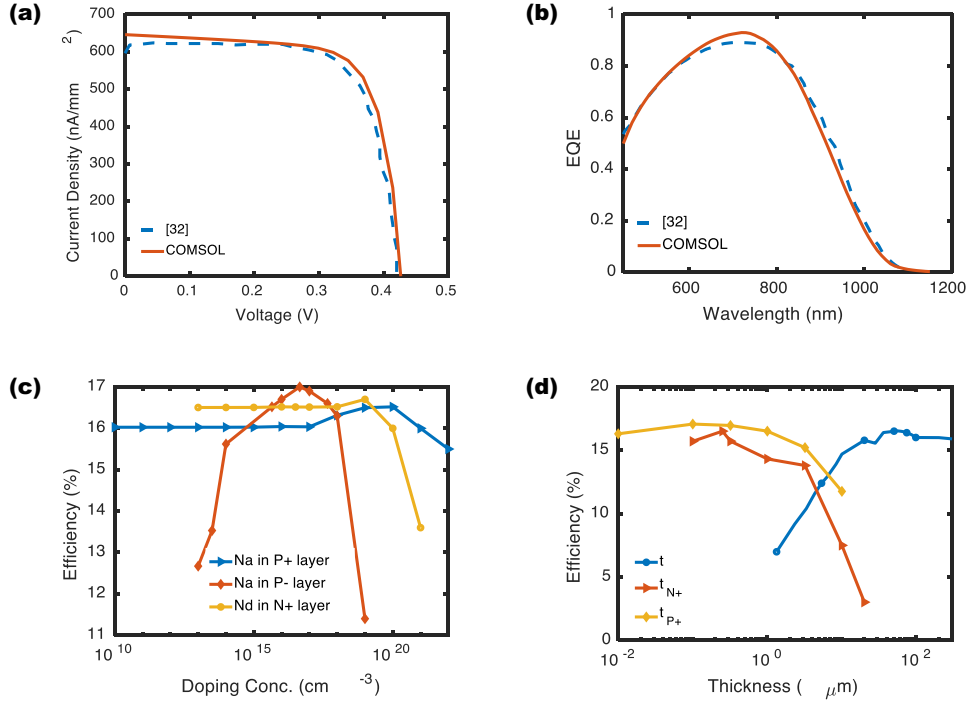
Fig. 2. The verified results with our model and [32]. (a) The JV curves of our model and [32] according to different forward bias condition. (b) The EQE value comparison between [32] and our model according to different spectra. The value shows great match between our simulation and experimental results in [32]. There are slightly difference in visible range and NIR range because the absorption profile of material [32][47] can be different from that in reality according to Eq. 3. (c) The efficiency change correlated to doping concentration in different solar cell layers. The results are achieved under one sun condition (100 mW/cm²), and thickness of P+ layer, N+ layer and P- layer are 1 μm, 0.25 μm and 50 μm. The optimal doping concentrations of the P+ layer, P- layer and N+ layer is 1×10^{20} cm^{-3}, 4.6×10^{15} cm^{-3} and 1×10^{16} cm^{-3}, respectively. (d) The efficiency changes with different layer thickness. The optimal thickness for the P+ layer, N+ layer and total device thickness are 0.1 μm, 0.25 μm and 56 μm under one sun condition with doping profile in Table I.

the thickness of each layer varies with different skin profiles. For example, the stratum corneum is ~10 μm, the epidermis is between 100 to 150 μm, the dermis is between 1 to 4 mm, and the hypodermis is between 1 mm to 6 mm [44]. Consequently, we apply a multi-layer skin structure by using a 10 μm stratum corneum, 100 μm epidermis, 1 mm dermis and 3 mm hypodermis, which is shown in Fig. 1. The propagation of light through the skin can be modelled using a 2×2 characteristic matrix [45]:

$$\begin{bmatrix} E_{Ra} \\ B_{Ra} \end{bmatrix} = \left\{ \sum_{i=1}^{m} \begin{bmatrix} \cos\varphi_i & (j/\eta_i)\sin\varphi_i \\ j\eta_i \sin\varphi_i & \cos\varphi_i \end{bmatrix} \right\} \begin{bmatrix} 1 \\ \eta_m \end{bmatrix} \quad (7)$$

where δ_i is the wave phase shift ($\delta_i = 2\pi N_i d_i \cos\theta_i / \lambda$) in the ith layer, N_i is the refractive index, d_i is the thickness of the ith layer, η_i is the pseudo index in i^{th} layer ($\eta_i = N_i \cos\theta_i$). E_{Ra} or B_{Ra} is the ratio between the (electric/magnetic) field of the transmitted light and the (electric/magnetic) field of the incident light. The reflectance (R), transmittance (T) and absorptance (A) of light can be determined using [45]:

$$T = \frac{4\eta_0 \, \text{Re}(\eta_m)}{(\eta_0 E_{Ra} + B_{Ra})(\eta_0 E_{Ra} + B_{Ra})^*} \quad (8a)$$

$$A = \frac{4\eta_0 \, \text{Re}(E_{Ra} B_{Ra}^* - \eta_m)}{(\eta_0 E_{Ra} + B_{Ra})(\eta_0 E_{Ra} + B_{Ra})^*} \quad (8b)$$

$$R + A + T = 1 \quad (8c)$$

II. MODEL VERIFICATION

Before device analysis and optimization, it is imperative to verify our model with experimental data. In this case, we setup a model of a single junction PV device using the parameters shown in Table I. The width and out-of-plane thickness of the cell are 1 mm and 1.22 mm respectively. We apply the analytical doping method to ensure a uniform doping concentration in each layer. The material properties are extracted from [46-54]. Comparisons between the reference cell [32] and simulations are shown in Figs. 2(a) and 2(b), demonstrating a good match between the results. The External Quantum Efficiency (EQE) of our model is high in both the visible and ultraviolet (UV) regions, due to the effective light reflections in both the front and rear planes. The JV curve shows a V_{oc} of 0.44 V and a J_{sc} of 650 nA/cm².

III. RESULTS AND DISCUSSION

In this section, we demonstrate the performance of our device in different skin layers. Initially, we optimized the device by changing the doping profile and geometry to improve the output performance using the parameters shown in Table I. The doping profile changes the band structure of the material, and the device performance is limited due to recombination losses, which reduces the open circuit voltage to less than the theoretical limit [32]. The thickness will affect the penetration of light, which will undoubtedly affect
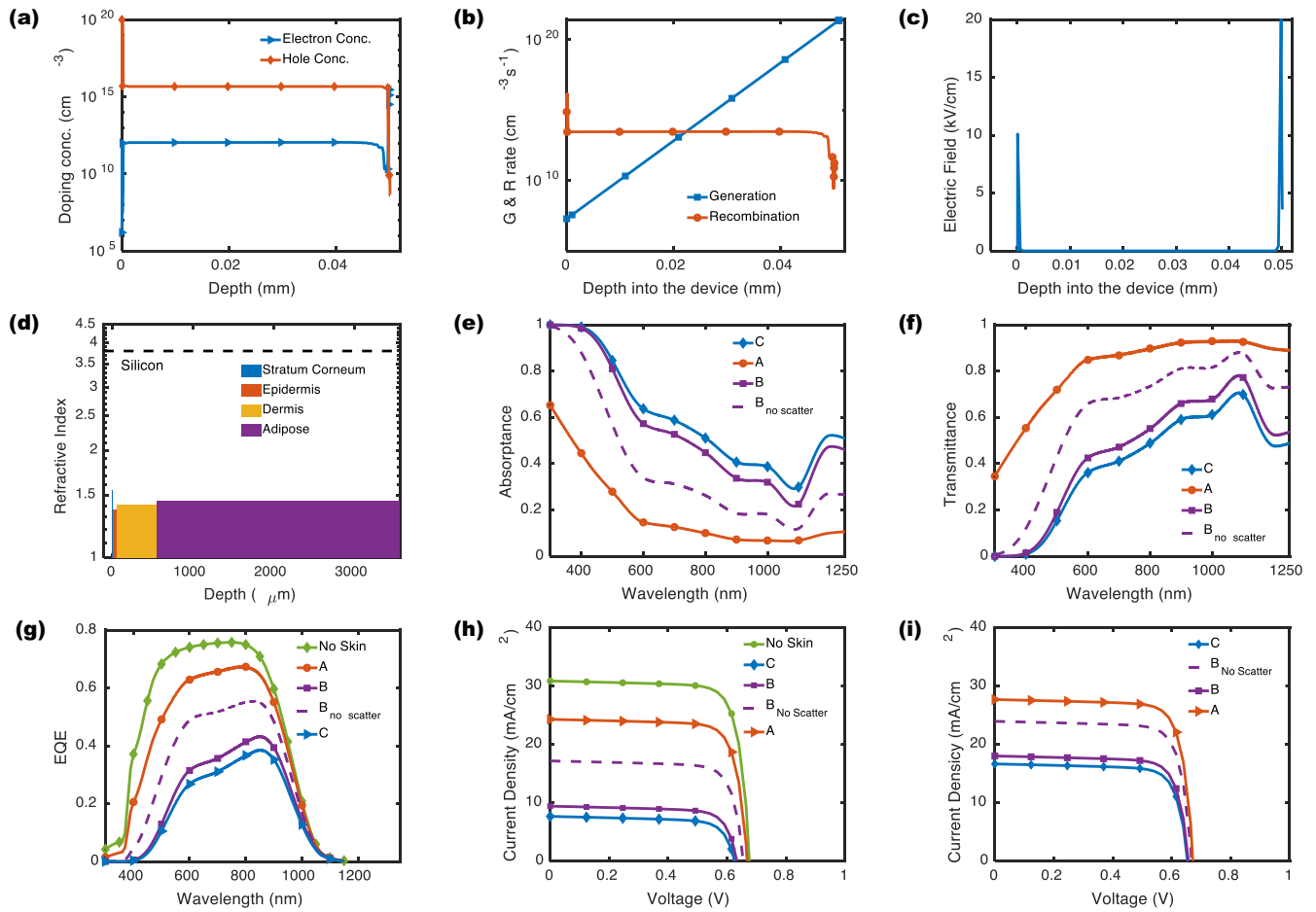
Fig. 3. (a) The doping profile in our device corresponds to depth. (b) The generation and recombination rate at 550 nm wavelength. (c) The electric field correlated to the depth into the PV cell. (d) The refractive index correlated to the depth in the skin model. The Absorptance (e) and Transmittance (f) of the multilayer structure with scattering consideration. The structure is composed of 10 µm stratum corneum, 100 µm epidermis, 1 mm dermis and 3 mm adipose (or hypodermis). It clearly shows that the transmittance of skin is dramatically degraded with scattering considered. The reflectance is neglected due to its small value (0.1%). Besides, it shows that the adipose layer causes less influence in light penetration into the tissue. (g) and (h) show the electric performance of the devices: EQE according to spectra, where the peak wavelengths are 750 nm (No skin), 800 nm (A), 832 nm (B without scattering), 850 nm (B) and 850 nm (C). and JV curves of different implanting location according to a wavelength of 550 nm. (i) shows the JV curves when the device is illuminated in peak wavelength obtained from Fig. 3(g), 100 mW/cm^2 @ 800 nm (A), 832 nm (B without scattering), 850 nm (B) and 850 nm (C).

the amount of photo-generated current. In our design, we sweep the doping profile of the base layer, front layer and back layer, and then check the efficiency changes. Based on the inset of Fig. 2 (c), optimal doping concentration for the base layer, front layer and back layer are 4.6×10^{15} cm^{-3}, 1×10^{19} cm^{-3} and 1×10^{20} cm^{-3}, respectively. For the doping concentration in the front layer, we can obtain the same efficiency of 16.5% at both 1×10^{16} cm^{-3} and 1×10^{18} cm^{-3}. However, we preferred the light doping solution to avoid possible defects as a result of excessive doping during fabrication. The efficiencies according to the thickness of the base layer, front layer and back layer are shown in Fig. 2 (d). Based on this, we can obtain the optimal thickness of each layer: 50 µm (Base), 0.25 µm (Front) and 0.1 µm (Back).

The baseline performance is shown in Fig. 3 under AM 1.5G condition (100 mW/cm^2). Our device can achieve 17.20 mW maximum power at 0.585 V with 17.20% efficiency. The open-circuit voltage is 0.675 V, and the short-circuit current density is 31.42 mA/cm^2, which is shown in Fig. 3(h) as 'No skin'. The EQE of our device is shown in Fig. 3(g), with a peak value of 75.80% at 750 nm.

The generation and recombination rates with a 550 nm light source are shown in Fig. 3(b), which is obtained using equations (3) and (4) without skin. The generation rate improves with the depth increased, while there is a trade-off point between the generation and recombination rates at a depth of 0.23 µm. The electrons are separated and accelerated in the junction boundaries, which are shown as the peak value in Fig. 3(c).

For illustration purposes, we demonstrate the refractive index of different skin layers in comparison to silicon PV cells, as shown in Fig. 3(d). Obviously, skin has almost one third the refractive index of silicon. Similarly, the absorptance and transmittance of light through skin are shown in Fig. 3(e) and Fig. 3(f), respectively. Overall, since light propagations through more tissue, there will be a greater amount of attenuation. The epidermis predominantly absorbs the light in the UV and visible regions, with 60% of light absorbed at 350 nm. The dermis can absorb almost 40% of light from all spectra except in the NIR region, where an average of 20% is absorbed. The influence of the adipose layer is less when compared to the other layers, and a 3 mm

TABLE II
COMPARISON TABLE WITH THE OTHER WORKS

Solar cells	Illumination	Skin type	Skin thickness	Output Power [a]	Reference
p-i-n Si	One Sun	Pork	3 mm	0.45 mW/cm^2 [b]	[25]
p-n GaAs	134 µW/cm^2 LED	Rat	4 mm	1.22 mW/cm^2 [c]	[32]
p-n Si	One Sun	Human inner arm	0.951 ± 0.335 mm	3.5 mW/cm^2 [d]	[43]
GaAs:GaInP	One Sun	Rat	675 µm	4.5 mW/cm^2 [e]	[55]
n-p-p Si	100 mW/cm^2 850nm IR light	Human outer arm	4 mm	8.35 mW/cm^2 [f]	This work

[a] Power density can vary according to different experimental conditions. The following indicates the references.
[b] Measured by using 3 mm pork skin in-vitro.
[c] Measured under 4 mm Rat skin in-vitro, and an LED light source.
[d] Measured by using fresh skin from human (Asian 95 years old) in 26 hours after death without embalming process.
[e] Measured in vivo using hairless rat.
[f] Simulated by using the measured in-vivo human skin properties from literature. The implant location is just under dermis.

adipose can only cause 7% attenuation of light at 550 nm, in comparison to 10% loss at 850 nm, respectively. The transmittance is inversely proportional to the skin absorptance due to the small skin reflectance (less than 3%).

Fig. 3(g) shows the EQE according to different implant layers. When the device is implanted in Test Point A, an EQE of 67.50% can be achieved at the peak wavelength of 800 nm. When implanted in Test Point B, an EQE of 55.60% (Scattered) and 43.30% (Non-scattered) can be achieved at the peak wavelength of 832 nm and 850 nm, respectively. When implanted in Test Point C, the EQE is 38.50% at the peak wavelength of 850 nm. Fig. 3(h) shows the JV characteristics under 1 Sun illumination conditions (i.e. 100 mW/cm^2 at 550 nm) when the device is implanted in a different layer of human tissue as well as without tissue. The short circuit current density, J_{sc}, decreases from 24.40 mA/cm^2 to 8.21 mA/cm^2, and the open circuit voltage, V_{oc}, decreases from 0.670 V to 0.620 V. Furthermore, the maximum power, P_{max}, can be determined using the JV curves in Figs. 3(h) and 3(i). The power therefore decreases from 13.36 ± 1 mW to 4.16 ± 1 mW. The skin transmittance influences the light illumination at the device surface, and the generation rate will be degraded according to the Eq. 4. The V_{oc} is related to the generation rate, which is qualitatively consistent with the decrease in V_{oc} (7.46%) [26]. Fig. 3(i) shows the JV characteristics at different test point when illuminated in the peak wavelength. Light attenuation through skin (Between A and C) causes 11 mA/cm^2 difference of J_{sc}, 0.02 V difference in V_{oc}, and 6.43 mW difference in P_{max}. The device will generate the highest amount of power in point B by illuminating it at the peak wavelength, which is 11.84 mW. Considering the power output, the dermis layer (between points A and B) is the best implant location, since it enables the PV cell to generate 15 mW for an 800 nm light source and 13 mW for a 550 nm source. However, depending upon the type of light source and the implantation depth, the amount of harvested power will vary. For example, if the device is implanted in the narrow region between points A and B, it will generate up to 8.57 mW for a white light source and 3.45 mW for NIR light. This region is typically 1mm in depth. However, if the device is implanted between points B and C, which is almost 3 mm, it will generate 0.63 mW for a white light source and 2.98 mW for NIR light. Consequently, we recommend

implanting our PV cells between regions B and C since it is thicker, which makes it easier to implant in the human body and the amount of harvested power is constant within this region. To overcome the high amount of attenuation, we recommend using NIR light.

Another phenomenon that affects the performance of our PV cells is light scattering, which may be due to blood and water content in the skin layers. By implanting the device in point B, scattering causes a 47% drop in power at 550 nm and 9% at 850 nm. Similarly, implanting the device in location C results in 28% drop using NIR light and 52% using white light. Table II compares our work with previously published work [25, 32, 43, 55]. Our proposed implantation location (between B and C), illumination wavelength (NIR light) and optimised PV cell clearly harvests higher power (> 8.35 mW/cm^2) than the literature. Despite of the comparison between the different PV cells, our cell can also compare with the other energy harvesters. For output voltage, PV cells are less restricted by the size of the organ or the depth of the implants compared with the other energy harvesters, which is shown in Figs. 3(h) and 3(i). In the system level, Some energy harvesters such as PEG, TENG and WPT are considered as an AC sources, while the implantable PV cell is considered as a DC source, relaxing the additional loss due to the extra AC-DC power conversion stage [8].

IV. CONCLUSION

We have demonstrated the performance of an implantable PV device using the FEM method. In our design, PV cells implanted in the adipose layer can harvest nearly 11.84 mW using an 850 nm light source. This power can drive implantable devices such as pacemakers and biomedical sensors. The epidermis layer absorbs most of the visible light, and the dermis layer absorbs most of the NIR light. We further concluded that the dermis layer is a good location for implantable PV cell to acquire a high-power output, and the adipose layer is an excellent location to obtain a stable power output. NIR light enables high skin transmittance and low scattering losses, which is beneficial for the PV cell, but may be hazardous for the human body due to possible heating effects. In future, we will investigate the effect of heat on the device performance, as well as the biocompatibility of the PV device with the human body. We will also investigate

the power transfer between the power harvester and load for the in-vitro tests after completing system integration and device encapsulation.

REFERENCES

[1] X. Liang, R. Ghannam, and H. Heidari, "Wrist-worn Gesture Sensing with Wearable Intelligence," *IEEE Sensors Journal,* vol. 19, no. 3, pp. 1082-1090, Feb. 2019.

[2] F.-G. Zeng, S. Rebscher, W. Harrison, X. Sun, and H. Feng, "Cochlear Implants: System Design, Integration, and Evaluation," *IEEE Reviews in Biomedical Engineering,* vol. 1, pp. 115-142, Nov. 2008.

[3] J. D. Weiland and M. S. Humayun, "Visual Prosthesis," *Proceedings of the IEEE,* vol. 96, no. 7, pp. 1076-1084, July 2008.

[4] R. B. North, "Neural Interface Devices: Spinal Cord Stimulation Technology," *Proceedings of the IEEE,* vol. 96, no. 7, pp. 1108-1119, July 2008.

[5] M. A. Lebedev and M. A. Nicolelis, "Brain–machine interfaces: past, present and future," *TRENDS in Neurosciences,* vol. 29, no. 9, pp. 536-546, Sept. 2006.

[6] J. P. DiMarco, "Implantable Cardioverter–Defibrillators," *New England Journal of Medicine,* vol. 349, no. 19, pp. 1836-1847, Nov. 2003.

[7] S. Zuo, K. Nazarpour, and H. Heidari, "Device Modeling of MgO-Barrier Tunneling Magnetoresistors for Hybrid Spintronic-CMOS," *IEEE Electron Device Letters,* vol. 39, no. 11, pp. 1784-1787, Nov. 2018.

[8] B. Shi, Z. Li, and Y. Fan, "Implantable Energy-Harvesting Devices," *Advanced Materials,* vol. 30, no. 44, p. 1801511, July 2018.

[9] J. Zhao, R. Ghannam, Q. H. Abbasi, M. Imran, and H. Heidari, "Simulation of Photovoltaic Cells for Implantable Sensory Applications," presented at the IEEE Sensors Conf., Oct., 2018.

[10] K. Oo Htet, R. Ghannam, Q. H. Abbasi, and H. Heidari, "Power Management Using Photovoltaic Cells for Implantable Devices," *IEEE Access,* vol. 6, pp. 42156 - 42164, Aug. 2018.

[11] K. O. Htet, J. Zhao, R. Ghannam, and H. Heidari, "Energy-Efficient Start-up Power Management for Batteryless Biomedical Implant Devices," in *IEEE Int. Conference on Electronics, Circuits and Systems (ICECS)*, pp. 597-600, Dec. 2018.

[12] S. Abdellatif, K. Kirah, R. Ghannam, A. Khalil, and W. Anis, "Enhancing the absorption capabilities of thin-film solar cells using sandwiched light trapping structures," *Applied optics,* vol. 54, no. 17, pp. 5534-5541, June 2015.

[13] B. Michel, N. Moll, and R. Ghannam, "Light-reflecting grating structure for photovoltaic devices," US 9,985,147, 29 May 2018.

[14] A. Polman, M. Knight, E. Garnett, B. Ehrler, and W. Sinke, "Photovoltaic materials: present efficiencies and future challenges," *Solar Energy,* vol. 352(6283), p. aad4424, 2018.

[15] K. Agarwal, R. Jegadeesan, Y.-X. Guo, and N. V. Thakor, "Wireless Power Transfer Strategies for Implantable Bioelectronics," *IEEE Reviews in Biomedical Engineering,* vol. 10, pp. 136-161, Mar. 2017.

[16] J. Zhao, R. Ghannam, M. Yuan, H. Tam, M. Imran, and H. Heidari, "Design, Test and Optimization of Inductive Coupled Coils for Implantable Biomedical Devices," *Journal of Low Power Electronics,* vol. 15, no. 1, Feb. 2019.

[17] Y. Yu et al., "Biocompatibility and In-vivo Operation of Implantable Mesoporous PVDF-Based Nanogenerators," *Nano Energy,* vol. 27, pp. 275-281, Sept. 2016.

[18] G. Zhang, M. Li, H. Li, Q. Wang, and S. Jiang, "Harvesting Energy from Human Activity: Ferroelectric Energy Harvesters for Portable, Implantable, and Biomedical Electronics," *Energy Technology,* vol. 6, no. 5, pp. 791-812, May 2018.

[19] S. Il Park et al., "Ultraminiaturized photovoltaic and radio frequency powered optoelectronic systems for wireless optogenetics," *Journal of Neural Engineering,* vol. 12, no. 5, p. 056002, July 2015.

[20] K. MacVittie et al., "From "Cyborg" Lobsters to A Pacemaker Powered by Implantable Biofuel Cells," *Energy & Environmental Science,* vol. 6, no. 1, pp. 81-86, Sept. 2012.

[21] J. Schwefel et al., "Wireless Communication by An Autonomous Self-Powered Cyborg Insect," *Journal of The Electrochemical Society,* vol. 161, no. 13, pp. H3113-H3116, Jan. 2015.

[22] K. Shoji, Y. Akiyama, M. Suzuki, N. Nakamura, H. Ohno, and K. Morishima, "Biofuel Cell Backpacked Insect and Its Application to Wireless Sensing," *Biosensors and Bioelectronics,* vol. 78, pp. 390-395, Apr. 2016.

[23] L. Halámková, J. Halámek, V. Bocharova, A. Szczupak, L. Alfonta, and E. Katz, "Implanted Biofuel Cell Operating in a Living Snail," *Journal of the American Chemical Society,* vol. 134, no. 11, pp. 5040-5043, Mar. 2012.

[24] A. Cadei, A. Dionisi, E. Sardini, and M. Serpelloni, "Kinetic and Thermal Energy Harvesters for Implantable Medical Devices and Biomedical Autonomous Sensors," *Measurement Science and Technology,* vol. 25, no. 1, p. 012003, Nov. 2013.

[25] T. Wu, J.-M. Redouté, and M. R. Yuce, "A Wireless Implantable Sensor Design With Subcutaneous Energy Harvesting for Long-Term IoT Healthcare Applications," *IEEE Access,* vol. 6, pp. 35801-35808, July 2018.

[26] L. Lu et al., "Biodegradable Monocrystalline Silicon Photovoltaic Microcells as Power Supplies for Transient Biomedical Implants," *Advanced Energy Materials,* vol. 8, no. 16, p. 1703035, June 2018.

[27] M. Yip, R. Jin, H. H. Nakajima, K. M. Stankovic, and A. P. Chandrakasan, "A fully-implantable cochlear implant SoC with piezoelectric middle-ear sensor and arbitrary waveform neural stimulation," *IEEE Journal of Solid-state Circuits,* vol. 50, no. 1, pp. 214-229, Jan. 2015.

[28] J. Katic, S. Rodriguez, and A. Rusu, "A High-Efficiency Energy Harvesting Interface for Implanted Biofuel Cell and Thermal Harvesters," *IEEE Transactions on Power Electronics,* vol. 33, no. 5, pp. 4125-4134, June 2017.

[29] A. A. Babadi, S. Bagheri, and S. B. A. Hamid, "Progress on implantable biofuel cell: Nano-carbon functionalization for enzyme immobilization enhancement," *Biosensors and Bioelectronics,* vol. 79, pp. 850-860, May 2016.

[30] M. Schormans, V. Valente, and A. Demosthenous, "Practical Inductive Link Design for Biomedical Wireless Power Transfer: A Tutorial," *IEEE Transactions on Biomedical Circuits and Systems,* vol. 12, no. 5, pp. 1112-1130, July 2018.

[31] Q. Shi, T. Wang, and C. Lee, "MEMS based broadband piezoelectric ultrasonic energy harvester (PUEH) for enabling self-powered implantable biomedical devices," *Scientific reports,* vol. 6, p. 24946, Apr. 2016.

[32] E. Moon, D. Blaauw, and J. D. Phillips, "Subcutaneous Photovoltaic Infrared Energy Harvesting for Bio-implantable Devices," *IEEE Transactions on Electron Devices,* vol. 64, no. 5, pp. 2432-2437, May 2017.

[33] Z. Chen, M.-K. Law, P.-I. Mak, and R. P. Martins, "A Single-Chip Solar Energy Harvesting IC Using Integrated Photodiodes for Biomedical Implant Applications," *IEEE Transactions on Biomedical Circuits and Systems,* vol. 11, no. 1, pp. 44-53, Feb. 2017.

[34] S. Ayazian, V. A. Akhavan, E. Soenen, and A. Hassibi, "A Photovoltaic-Driven and Energy-Autonomous CMOS Implantable Sensor," *IEEE Transactions on Biomedical Circuits and Systems,* vol. 6, no. 4, pp. 336-343, Aug. 2012.

[35] Y. Hung, Jr. et al., "High-Voltage Backside-Illuminated CMOS Photovoltaic Module for Powering Implantable Temperature Sensors," *IEEE Journal of Photovoltaics,* vol. 8, no. 1, pp. 342-347, Jan. 2018.

[36] E. Moon, D. Blaauw, and J. D. Phillips, "Small-Area Si Photovoltaics for Low-Flux Infrared Energy Harvesting," *IEEE Transactions on Electron Devices,* vol. 64, no. 1, pp. 15-20, Jan. 2017.

[37] S.-H. Tseng, A. Grant, and A. J. Durkin, "In Vivo Determination of Skin Near-infrared Optical Properties Using Diffuse Optical Spectroscopy," *Journal of Biomedical Optics,* vol. 13, no. 1, p. 014016, Jan. 2008.

[38] S. L. Jacques, "Optical Properties of Biological Tissues: A Review," *Physics in Medicine & Biology,* vol. 58, no. 11, p. R37, May 2013.

[39] W. Cheong, S. Prahl, and A. Welch, "A Review of the Optical Properties of Biological Tissues," *IEEE J. Quantum Electron,* vol. 26, no. 12, pp. 2166-2185, Dec. 1990.

[40] C. Yan and P. S. Lee, "Stretchable Energy Storage and Conversion Devices," *Small,* vol. 10, no. 17, pp. 3443-3460, Sept. 2014.

[41] X. Li, N. P. Hylton, V. Giannini, K. H. Lee, N. J. Ekins-Daukes, and S. A. Maier, "Multi-dimensional Modeling of Solar Cells with Electromagnetic and Carrier Transport Calculations," *Progress in Photovoltaics: Research and Applications,* vol. 21, no. 1, pp. 109-120, Jan. 2013.

[42] P. P. Altermatt, "Models for Numerical Device Simulations of Crystalline Silicon Solar Cells—A Review," *Journal of Computational Electronics,* vol. 10, no. 3, p. 314, Sept. 2011.

[43] K. Song, J. H. Han, H. C. Yang, K. I. Nam, and J. Lee, "Generation of electrical power under human skin by subdermal solar cell arrays for implantable bioelectronic devices," *Biosensors & Bioelectronics,* vol. 92, pp. 364-371, June 2017.

[44] A. N. Bashkatov, E. A. Genina, and V. V. Tuchin, "Optical Properties of Skin, Subcutaneous, and Muscle Tissues: A Review," *Journal of Innovative Optical Health Sciences,* vol. 4, no. 01, pp. 9-38, Jan. 2011.

[45] H. A. Macleod and H. A. Macleod, *Thin-film optical filters*. CRC press, 2010.

[46] W. Gerlach, H. Schlangenotto, and H. Maeder, "On the Radiative Recombination Rate in Silicon," *Physica status Solidi (a),* vol. 13, no. 1, pp. 277-283, Sept. 1972.

[47] A. Dargys and J. Kundrotas, *Handbook on Physical Properties of Ge, Si, GaAs and InP*. Science and Encyclopedia Publ., 1994.

[48] A. S. Grove, *Physics and Technology of Semiconductor Devices*. Wiley, 1967.

[49] A. Okhotin, A. Pushkarskii, and V. Gorbachev, "Thermophysical Properties of Semiconductors, Atom Publ," *House, Moscow,* 1972.

[50] M. A. Green, "Self-Consistent Optical Parameters of Intrinsic Silicon at 300 K Including Temperature Coefficients," *Solar Energy Materials and Solar Cells,* vol. 92, no. 11, pp. 1305-1310, Nov. 2008.

[51] S. O. Kasap, *Principles of Electronic Materials and Devices*. McGraw-Hill New York, 2006.

[52] M. Tyagi and R. Van Overstraeten, "Minority Carrier Recombination in Heavily-Doped Silicon," *Solid-State Electronics,* vol. 26, no. 6, pp. 577-597, June 1983.

[53] J. A. del Alamo and R. M. Swanson, "Modelling of Minority-Carrier Transport in Heavily Doped Silicon Emitters," *Solid-State Electronics,* vol. 30, no. 11, pp. 1127-1136, Nov. 1987.

[54] J. Dziewior and W. Schmid, "Auger Coefficients for Highly Doped and Highly Excited Silicon," *Applied Physics Letters,* vol. 31, no. 5, pp. 346-348, Sept. 1977.

[55] K. Song *et al.*, "Subdermal Flexible Solar Cell Arrays for Powering Medical Electronic Implants," *Advanced Healthcare Materials,* vol. 5, no. 13, pp. 1572-1580, July 2016.